Draft of Mar. 23, 2021

Published as:

Cecil MR, Gehrels GE, Rusmore ME, Woodsworth GJ, Stowell HH, Yokelson IN, Homan E, Kitajima K, Valley JW (2021) Mantle control on magmatic flare-ups in the southern Coast Mountains batholith, British Columbia . Geosphere, 15 p., doi.org/10.1130/GES02361.1.

Mantle control on magmatic flare-ups in the southern Coast Mountains batholith, British Columbia

Cecil, M. Robinson[1]*, Gehrels, George E.[2], Rusmore, Margaret E.[3], Woodsworth, Glenn J.[4], Stowell, Harold H.[5], Yokelson, Intan N.[2], Homan, Emily[1], Kitajima, Kouki[6], Valley, John W.[6]

[1]*Department of Geological Sciences, California State University, Northridge, Northridge, CA 91130*

[2]*Department of Geosciences, University of Arizona, Tucson, AZ 85721*

[3]*Department of Geology, Occidental College, Los Angeles, CA 90041*

[4]*Geological Survey of Canada, Vancouver, Canada*

[5]*Department of Geological Sciences, University of Alabama, Tuscaloosa, AL 35401*

[6]*Department of Geoscience, University of Wisconsin, Madison, WI 53706*

**corresponding author. Email: robinson.cecil@csun.edu*

ABSTRACT

The southern Coast Mountain batholith (CMB) was episodically active from Jurassic to Eocene time, experiencing four distinct high magmatic flux events during that period. Similar episodicity has been recognized in arcs worldwide, yet the mechanism(s) driving such punctuated magmatic behavior are debated. This study uses zircon Hf and O isotopes, together with whole rock and mineral geochemistry, to track spatiotemporal changes in southern CMB melt sources and to evaluate models of flare-up behavior and crust formation in Cordilleran arc systems. Zircon Hf isotope analysis yielded consistently primitive values, with all zircon grains recording initial εHf between +6 and +16. The majority (97 %) of analyzed zircons yielded $\delta^{18}O$ values between 4.2 and 6.5 ‰, with only 5 grains recording values up to 8.3‰. These isotopic results are interpreted as reflecting magmatism dominated by mantle melting, during all time periods and across all areas of the southern batholith, which argues against the periodic input of more melt-fertile crustal materials as the driver of episodic arc magmatism. They also indicate that limited crustal recycling is needed to produce the large volumes of continental crust generated in the batholith. Although the isotopic character of intrusions is relatively invariant through time, magmas emplaced during flare-ups record higher Sr/Y and $La/Yb_{(N)}$ and lower zircon Ti and Yb concentrations, consistent with melting in thickened crust with garnet present as a fractionating phase. Flare-ups are also temporally associated with periods when the southern Coast Mountains batholith advances inboard. We suggest that migration of the arc into more fertile lithospheric mantle domains triggers voluminous magmatism and is accompanied by tectonic and magmatic thickening. Overall, these results demonstrate that the magmatic growth of Cordilleran arcs can be spatially and temporally complex without requiring variability in the contributions of crust and / or mantle to the batholith.

INTRODUCTION

Continental arcs are important sites of continental crust generation and modification and the large composite batholiths produced in arcs record the combined processes of partial mantle melting and crustal recycling. Most continental, or Cordilleran-type, arcs are constructed over long periods of time (≥ 100 Myr), and although subduction may be ongoing over those intervals, magmatism appears to be highly episodic (e.g. Armstrong, 1988; Ducea, 2001; Paterson and Ducea, 2015). This episodic behavior is characterized by high-flux magmatic events, or "flare-ups" that quasi-periodically punctuate the baseline rates of magmatism. The processes that control the oscillation of arcs between flare-up and baseline modes remain debated, but are generally thought to be either internal to the arc (i.e. tectono-magmatic processes operating in the upper plate such as periodic crustal thickening or delamination) or external to the arc (e.g. periodic change in the obliquity or rate of plate convergence). Flare-ups are capable of producing as much as 90% of the magmatic additions to arcs (Ducea and Barton, 2007) and therefore identifying the petro-tectonic mechanisms that control them is critical to our understanding of the growth of continental crust both in individual arc systems, as well as globally.

Isotopic investigation of plutons in many Cordilleran arcs, particularly those emplaced along the margins of North and South America, has revealed significant incorporation (up to 50%; Ducea et al., 2015) of preexisting upper plate lithosphere in new arc melts. This process is evidenced by higher $^{87}Sr/^{86}Sr$ and lower εNd and εHf in batholithic rocks, all of which point to the incorporation of older, upper plate materials in magma sources, though cannot be used to distinguish between contributions from crustal and mantle lithospheric components. Recycling of crust is reflected in the $\delta^{18}O$ of igneous materials elevated above mantle values, which can only occur if surficial rocks that have isotopically exchanged with the hydrosphere are partially melted

(Valley et al., 2005). Examples of these isotopic systems being interpreted to indicate upper plate recycling have been documented in the Sierra Nevada (Lackey et al., 2008; 2012; Cecil et al., 2012), the Peninsular Ranges batholith (Kistler et al., 2014), the Idaho batholith (King and Valley, 2001; Gashnig et al., 2011), and the Coast Mountains batholith (Samson et al., 1991; Wetmore and Ducea, 2011; Cecil et al., 2011; Girardi et al., 2012). Furthermore, upper plate additions into batholithic melts have been temporally linked to high-flux events (e.g. Ducea and Barton, 2007), leading to models wherein arc flare-ups are fueled by the periodic incorporation of more melt-fertile, crustal materials (Ducea and Barton, 2007; DeCelles et al., 2009). In contrast, several recent studies have suggested that flare-ups are dominated by juvenile melts and driven by episodic events in the mantle (Decker et al., 2017; Martínez Ardila et al., 2019; Attia et al., 2020). In these cases, moderately depleted εNd and εHf signatures are attributed to contributions from enriched mantle sources.

The primary goals of this study are to test the possibility that magmatic flare-ups in the Coast Mountains batholith (CMB) are driven by the episodic addition of supracrustal materials to melt sources and to develop a petro-tectonic model to explain the complex spatio-temporal magmatic patterns observed in the batholith. The southern part of the batholith is an interesting and ideal site for this test because it provides continuous, arc-perpendicular exposures of intrusive rocks that have variable compositions and that span the lifetime of the active arc. Geochronologic analysis of these intrusions revealed a complex, episodic magmatic history, and one that is distinct from the batholith to the north, yet the processes controlling arc tempos remain uncertain (Cecil et al., 2018). It appears that magmatism is at times – but not always – synchronous with periods of crustal deformation (Rusmore et al., 2013, 2019) and metamorphism (Bollen et al., *in review;* Dafov et al., 2020). By investigating the geochemical and isotopic compositions of Jurassic –

93 Eocene intrusions of the southern CMB, we can evaluate: 1) the extent to which crust and mantle
94 sources are involved in batholith generation through time and space; 2) the depth and thermal
95 conditions of melt generation; and 3) links between magmatism, deformation and metamorphism.
96 Our results indicate that magmatism in the southern CMB is dominated by mantle melting,
97 as recorded in primitive zircon εHf and uniformly mantle-like zircon $\delta^{18}O$ values. Input of older
98 and / or near-surface country rocks is limited, indicating that melt-fertile supracrustal materials
99 cannot be the primary drivers of magmatic flare-ups. Crustal recycling is therefore not likely to be
100 a volumetrically significant process within the southern CMB, which instead reflects the
101 generation of new continental crust (Hollister and Andronicos, 2006). The processes controlling
102 mantle-driven flare-ups remain uncertain, but spatial and temporal trends in the geochronologic
103 and geochemical data suggest that periodic inboard advance of the Coast Mountains arc may lead
104 to episodic tapping of more fertile sub-continental mantle lithosphere, producing the mantle-like
105 flare-ups observed.
106
107 GEOLOGIC AND TECTONIC FRAMEWORK
108 The Coast Mountains batholith is one of the largest exposed Cordilleran arcs, extending >
109 1500 km along the western margin of southeast Alaska and British Columbia. Subduction of paleo-
110 Pacific plates beneath western North America drove the nearly continuous growth of the batholith
111 for ~ 150 m.y. in Jurassic to early Eocene time, whereupon the margin began transitioning to a
112 dextral transform system (e.g. Stock and Molnar, 1988; Madsen et al., 2006). The southern part of
113 the Coast Mountains batholith investigated as part of this study is exposed between ~ 50.5 and 52
114 °N (Fig. 1). This is one of the widest parts of the batholith, with very little host rock exposed,
115 making the affinity of the basement into which the southern CMB is emplaced uncertain.

Vancouver Island, which comprises rocks of the Wrangellia terrane, is located to the west of the study area, whereas Triassic – Cretaceous rocks of the Intermontane superterrane outcrop to the east; the location of the boundary between the two is unknown. Paleomagnetic results, together with patterns observed from geochronologic datasets, suggest that the Intermontane superterrane may extend westward to Vancouver Island, underlying much of the batholith at the study latitudes (Rusmore et al., 2013). This is also consistent with recent detrital zircon results from metasedimentary pendants preserved in Bute and Knight Inlets (Dafov et al., 2020).

Magmatic history

The southern CMB was emplaced between ca. 170 – 45 Ma, and although magmatism was continuous during that time, the rates of magmatic addition to the batholith varied considerably. The southern batholith experienced 4 magmatic flare-up events at 161-148 Ma, 114-102 Ma, 85-70 Ma, and 61-48 Ma, with intervening apparent magmatic lulls at 148-114 Ma, 102-85 Ma, and 70-61 Ma (Cecil et al., 2018). The Jurassic event coincides with a Cordilleran arc flare-up documented along most of the North American margin (Gehrels et al., 2009; Kirsch et al., 2016; Beranek et al., 2017). The timing of Cretaceous and Paleocene – Eocene high flare-ups differs from those documented in the central and northern parts of the batholith (Gehrels et al., 2009), which suggests a relatively small-scale (i.e. not plate-scale) control on high-volume magmatic events (de Silva et al., 2015; Kirsch et al., 2016; Cecil et al., 2018). Jurassic to Early Cretaceous intrusions are restricted to the western part of the southern CMB and magmatism generally becomes younger to the east, such that post-80 Ma plutons are only found at distances greater than 100 km inboard from the coastline. Eastward migration of the post-mid-Cretaceous CMB has been recognized along the length of the arc, and although arc migration rates have been estimated at

between 2.1 to 2.8 km/Ma for all arc segments, the spatial evolution of arc magmatism may be more complex than previously recognized (Gehrels et al., 2009; Cecil et al., 2018).

METHODS

Whole-rock geochemistry

Many of the intrusions analyzed in this study are the same as those dated and discussed in Cecil et al. (2018). Sample information and location data is provided in Supplementary Data Table 1. During the zircon separation process, ~ 10 gm aliquots of crushed rock were set aside for whole rock geochemical analysis. Additional hand samples of large or complex plutons were also collected and crushed in order to characterize the geochemistry of potentially heterogeneous intrusions. Unweathered rock chips selected from crushed whole rock samples were powdered in an alumina ceramic ring and puck mill and analyzed for major and trace elements either via X-Ray Fluorescence (XRF) at Pomona College or by inductively-coupled plasma mass spectrometry (ICPMS) at Activation Laboratories (Ontario, Canada). Samples analyzed by XRF at Pomona College were also digested in acid and then analyzed for rare earth elements by ICPMS at California State University, Northridge (CSUN). All whole-rock geochemical data and modes of analysis are given in Supplementary Data Table 2.

Zircon Hf isotope analysis

Hafnium isotope analysis was performed on dated zircon grains via laser-ablation (LA)-ICPMS at the Arizona LaserChron Center using a Nu Instruments multi-collector mass spectrometer coupled with a Photon Machines Analyte G2 excimer laser system. The analytical procedures, and mass bias and interference corrections used follow those described in Cecil et al.

(2011) and Gehrels and Pecha (2014). Hafnium isotope data were acquired for a total of 775 zircons from 54 plutonic samples. These analyses are representative subsets (~ 10 - 15 grains per sample) of the same zircons dated as part of Cecil et al. (2018). Most zircon analyses reported in Cecil et al (2018) exhibited simple U-Pb systematics and did not display evidence of inheritance or overgrowths, as reflected in discrepant ages or unusual textures in cathodoluminescence (CL) images (e.g. thin, bright rims or cores with morphologies different that those of the crystal's external shape) (Fig. 2). Nevertheless, only zircons that were concordant, had CL textures interpreted to be magmatic (oscillatory or sector zonation), and contained only a single age domain, were analyzed. Wherever possible, Hf analysis was performed on top of existing U-Pb ablation pits in order to ensure the greatest likelihood of analyzing the same age domain sampled for U-Pb geochronology. Hafnium isotopic data for individual grain analyses are given in Supplementary Data Table 3.

Zircon O isotope analysis

Following zircon U-Pb and Hf isotope analysis, a subset of 22 samples were chosen for O isotope and trace element analysis of zircon. Samples were selected from all age groups and from a wide variety of locations and rock compositions in order to broadly characterize the CMB in our study area. New mounts were prepared from existing zircon separates and imaged by SEM-CL. Therefore, age and Hf isotope information cannot be directly connected to a given O isotope zircon analysis spot. However, given the intra-sample homogeneity of U-Pb ages and Hf isotope ratios (see Fig. 2), we are reasonably confident that the measured O isotope values correspond to previously-measured average U-Pb-Hf characteristics of a given intrusion. Oxygen isotope analyses were performed using a CAMECA IMS-1280 ion microprobe at the University of

Wisconsin-Madison, following procedures described in detail elsewhere (Kita et al., 2009; Valley and Kita, 2009). In summary: a $^{133}Cs^{+}$ primary beam (~2nA) was focused to ~10-micron spots on the polished zircon surface; three FC detectors simultaneously analyzed $^{16}O^{-}$, $^{16}OH^{-}$ and $^{18}O^{-}$; and eight analyses of KIM-5 zircon standard (Valley, 2003) bracket every 10-20 sample analyses. Values of $\delta^{18}O$ are reported in standard permil notation relative to VSMOW. Ratios of OH/O, corrected for background, were monitored as an indication of inclusions or radiation damage (Wang et al., 2014), which resulted in the rejection of 2 out of 175 analyses. The average spot-to-spot reproducibility (external precision) for $\delta^{18}O$ on KIM-5 for brackets of eight analyses is 0.19‰ (2SD). Oxygen isotope data for individual-grain analyses are given in Supplementary Data Table 4.

Zircon trace element analysis

Zircon trace element analysis was performed on the same sample subset as those for which O isotope data were obtained. Approximately 15 grains for each of the 22 samples were analyzed, for a total of 359 analyses. Trace element data were collected via LA-ICPMS at the University of Arizona LaserChron Center using a Photon Machines G2 excimer laser-ablation (LA) system coupled to a Thermo Fisher Scientific Element2 high resolution single collector ICPMS. A total of 24 different masses were analyzed, including the rare earth elements (REE), as well as P, Ti, Nb, Hf, Ta, Pb, U and Th. The natural zircon standard 91500 (Wiedenbeck et al., 2004) was used as a primary standard for calculating concentrations for all elements except for Ti, which was standardized using NIST 612 glass. Analytical methods and data reduction protocols used were the same as those described in Chapman et al. (2016). Trace element data for individual zircon analyses are given in Supplementary Data Table 5.

208

209 RESULTS

210 *Major and trace element geochemistry*

211 Whole-rock geochemical data were generated for 96 samples collected from intrusive rocks
212 of the southern CMB. Pluton compositions range from gabbro to granite, though the majority of
213 the batholith is composed of tonalite and granodiorite with SiO_2 contents > 65% (Fig. 3A). Plutons
214 emplaced during the most recent magmatic event in the arc, at 64-45 Ma, have higher average SiO_2
215 (68.3% SiO_2, compared with an overall average of 64.9% SiO_2), and are restricted to the
216 easternmost part of the southern batholith. Southern CMB intrusions are metaluminous to mildly
217 peraluminous (ASI = A/CNK = 0.8 – 1.15) and show a smooth trend of increasing alumina
218 saturation index (ASI) with increasing SiO_2 (Fig. 3B). Overall, major element data show that this
219 part of the batholith is magnesian, calcic to calc-alkalic and generally similar to rocks of the central
220 CMB (Girardi et al., 2012) and other Cordilleran arc granitoids (Frost et al., 2001) (Fig. 3).

221 Although major element data reveal little spatio-temporal variability in pluton
222 composition, there are changes in both La/Yb and Sr/Y through time. In general, plutons emplaced
223 during high-flux magmatic events have elevated La/Yb and Sr/Y, whereas those emplaced during
224 periods of relative arc inactivity do not (Fig. 4). For example, 46% of intrusions with ages
225 corresponding to a documented flare-up period have Sr/Y > 50, compared with only 12% of
226 intrusions emplaced during magmatic lulls.

227

228 *Zircon Hf and O isotope compositions*

229 Initial εHf values in CMB intrusions range from ~ +6 – +16, clustering around a mean of
230 +11.4 ± 1.9 and are distinct from the distribution of $\varepsilon Hf_{(t)}$ values documented in the central and

231 northern parts of the batholith (Cecil et al., 2011) (Fig. 5A). Samples from all age groups have
232 zircons that overlap with depleted mantle values. There are no obvious arc perpendicular trends
233 observed in the Hf isotope data, though plutons with the lowest average values (+7.7 to +8.9) are
234 found in axial arc positions and roughly coincide with a NW-trending package of gneisses.
235 Temporal trends in the Hf data are equally unclear. A running mean calculated for post-145 Ma
236 $\varepsilon Hf_{(t)}$ values reveals limited variability, with mean values ranging between ~ +11 and +13 (Fig. 6).
237 Contouring of individual Hf data points, however, does show values scattering to lower $\varepsilon Hf_{(t)}$
238 values at ca. 155 - 145 Ma, a time during which a high magmatic flux event is documented for the
239 CMB and most other segments of the North American Cordillera (Gehrels et al., 2009; Kirsch et
240 al., 2016; Berenek et al., 2017; Cecil et al., 2018).
241 Zircon $\delta^{18}O$ values from intrusive rocks of the southern CMB range from +4.2 to +8.3 ‰,
242 though the majority of analyzed grains cluster between +5 and +6 ‰, with an average of +5.4 ±
243 0.6 ‰ (1s) (Fig. 5B). Average $\delta^{18}O$ values for all analyzed plutons overlap with the accepted range
244 of mantle values (5.3 ± 0.6 ‰ (2s); Valley et al., 2005). Because of the relative invariability of the
245 zircon $\delta^{18}O$ data, they do not reveal any obvious spatial or temporal trends.
246
247 *Zircon trace element geochemistry*
248 Chondrite-normalized rare earth element (REE) trends in southern CMB zircons show
249 typical patterns of increasing concentration from light to heavy REEs, with marked positive-Ce
250 and negative-Eu anomalies (Fig. 7A). There are no significant changes in these trends (e.g.
251 steepness of heavy REE pattern, size of Ce or Eu anomaly, etc.) through time or space. The
252 majority (95%) of zircons from southern CMB plutons yield U/Th ratios <10; most of the 5% of
253 grains with U/Th ratios >10 have corresponding U-Pb ages of ~ 140 – 150 Ma (not shown), which

is also a pattern observed in metamorphic rims of detrital zircons in metasedimentary country rocks (Dafov et al., 2020). Hafnium concentrations range from 7,000 – 14,000 ppm, are positively correlated with U/Yb, and are generally very similar in their Hf and U/Yb variation to globally-compiled data for continental arcs (Fig. 7B) (Grimes et al., 2015). A bivariate plot of Ti vs Yb concentration again shows that our CMB zircon data are generally very similar to arcs worldwide, but also reveals a suggestion that intrusions crystallizing during interpreted flare-up events trend toward lower Ti and Yb (Fig. 7C).

DISCUSSION

Isotopic evidence for mantle-dominated batholith sourcing

Intrusive rocks comprising the southern CMB have zircon $\varepsilon Hf_{(t)}$ and $\delta^{18}O$ values that are relatively invariant and that overlap with documented mantle values for both isotopic systems (Fig. 5). Zircon $\delta^{18}O$ sample averages range from 4.5 to 6.4 ‰ and, in all cases, overlap within analytical error the range of accepted values for the high-temperature mantle (5.3 ± 0.6 ‰; Valley et al., 2005). Zircon $\varepsilon Hf_{(t)}$ values are positive and high (between ~ +6 and + 16), compatible with melting of a Lu-rich mantle source. In all geographic areas and in all stages of batholith development – apart from the Eocene, for which we have relatively little data – individual $\varepsilon Hf_{(t)}$ values overlap with the evolution of depleted mantle (Vervoort and Blichert-Toft, 1999; Dhuime et al., 2011) (Fig. 6). Although these data do not uniquely signify a mantle source, they do require melting of materials that have not exchanged with $\delta^{18}O$-enriched surface fluids, and that are young, and therefore characterized by juvenile εHf values. The isotopic data presented here are therefore consistent with partial melting of variably-enriched mantle, secondary melting of mantle-derived mafic underplates (Collins et al., 2020), remelting of juvenile arc crust, or a mixture thereof. The

bulk isotope modeling presented below, together with the isotopic homogeneity and the lack of zircon inheritance observed indicates that remelting of lower crustal arc terranes likely played an insignificant role.

The remarkable inter- and intra-sample uniformity observed in both the Hf and O datasets is one of the most distinctive features of the southern CMB and suggests batholith generation from a single, relatively homogeneous source. Zircon $\delta^{18}O$ values cluster tightly around a mean value of 5.4 ‰ (Fig. 5b), and although slightly more heterogeneous, zircon $\varepsilon Hf_{(t)}$ sample averages comprise a range of only 7 epsilon units (Fig. 6). Even intrusions with SiO_2 contents > 70% yield homogeneous, mantle-like values (ex: 14IY11 has SiO_2 = 71.2% and $\varepsilon Hf_{(t)}$ =13.3), suggesting that fractionation of a mantle partial melt, in the absence of crustal assimilation, is sufficient to explain most of the isotope data. These results are intriguing, given the large geographic area over which the southern batholith was sampled (> 15,000 km^2; Fig. 1) and the large variability in pluton composition (Fig. 3).

Despite the overall isotopically primitive signature recorded in the zircon data, some deviation from purely mantle-derived melts is observed. There is a slight pull-down in $\varepsilon Hf_{(t)}$ values at ca. 150 Ma, and perhaps another less defined pull-down at ca. 110 Ma (Fig. 6). Only in these times do average pluton $\varepsilon Hf_{(t)}$ values move out of the "juvenile", and into the "moderately juvenile" fields, defined by Bahlburg et al. (2011) as reflecting partial melts of sources that were extracted from the mantle 0-300 m.y.a., and 300 – 650 m.y.a., respectively. Therefore, although there is little evidence for significant contributions of Precambrian crust to southern CMB melts, contamination by small amounts of relatively young (Phanerozoic) crust is permissible. This contamination may be evident in Jurassic samples that have lower average $\varepsilon Hf_{(t)}$ and zircons with slightly elevated $\delta^{18}O$ (+5.5 to + 6.8 ‰), with one sample (14IY25, from Bute Inlet) containing a

300 single grain with measured $\delta^{18}O$ of +8.3 ‰. The amount and nature of the crustal-end-member
301 contaminant permitted by our isotope data is explored in the next sections using a compilation of
302 available Hf isotope data from CMB basement terranes, and Hf-O bulk mixture models.
303
304 *Incorporation of probable host rocks into batholithic melts?*
305 Modelling of the potential crustal component is hindered by uncertainty as to the rocks
306 underlying much of the southern Coast Mountains batholith. Sparse pendants of weakly to strongly
307 metamorphosed volcanic and sedimentary rocks have traditionally been considered part of
308 Wrangellia, a terrane well-exposed on Vancouver Island and the westernmost mainland (Nelson,
309 1979; Monger et al., 1982; Wheeler and McFeely, 1991). In contrast, magmatic patterns and
310 paleomagnetic results suggest that the CMB at the study latitudes is emplaced into Intermontane
311 (likely Stikine) terrane (Rusmore et al., 2013). Detrital zircon data from recent work on
312 metasedimentary pendants in the southern batholith generally supports that interpretation, but are
313 also compatible with connection to Wrangellia terrane and possibly Alexander terrane, as exposed
314 in the Banks Island region to the northwest (Dafov et al., 2020). We approach estimating the
315 contributions of partial melts of these terranes into CMB magmas through bulk mixture modeling
316 of zircon Hf-O, with the understanding that this modeling is hampered by the fact that the isotopic
317 compositions of the crustal end members are poorly known.
318 Stikine terrane is composed primarily of Late Paleozoic through Jurassic island arc-related
319 volcanics with juvenile isotopic signatures (Dostal et al., 1999, 2009; Barresi et al., 2015). These
320 arc rocks overlie and / or interfinger with carbonates and siliciclastic rocks (Nelson et al., 2006)
321 thought to have been deposited on pericratonic basement (Jackson et al., 1991; Gehrels and Kapp,
322 1998). Wrangellia terrane, as exposed on Vancouver Island, is dominated by Paleozoic and

323 Mesozoic igneous rocks, including Devonian – Mississippian bimodal volcanics of the Sicker
324 Group and similarly-aged intrusives of the Saltspring Suite (Ruks, 2015), extensive Triassic basalts
325 of the Karmutsen Formation (Greene et al., 2009) and Jurassic bimodal volcanics and intrusives
326 of the Bonanza arc (DeBari et al., 1999). Also present are chert, argillite, limestone and minor
327 clastics of the lower Paleozoic Sicker Group and the upper Paleozoic Buttle Lake Group (Brandon
328 et al., 1986; Massey and Friday, 1989; Yorath et al., 1999). The southern part of the Alexander
329 terrane (Banks Island region) consists of Ordovician to Permian quartzite, marble and metapelite
330 assemblages (Tochilin et al., 2014).

331 Bulk mixture modeling is used to assess the extent to which assimilation of these probable
332 crustal contaminants (Wrangellia, Alexander, Stikine) is permitted based on the zircon Hf-O data.
333 Results of that modeling are shown in Figure 8. Based on the dominantly igneous nature of
334 Wrangellia and Stikine terranes, both of which contain young, hydrothermally altered oceanic
335 crust and volcaniclastic sedimentary rocks, we group them together and assign them a minimum
336 zircon $\delta^{18}O$ of ~ +10 ‰, similar to zircon $\delta^{18}O$ values assumed for accreted ocean arc terranes in
337 the Sierra Nevada foothills (Lackey et al., 2012). On the basis of available zircon Hf data for
338 Wrangellia (Alberts et al., 2021), whole rock Nd from local metasedimentary pendants (Bollen et
339 al., *in review*) and whole rock Nd for rocks of Stikine (Samson et al., 1989; Jackson et al., 1991),
340 $\varepsilon Hf_{(100\ Ma)}$ of these terranes is estimated to be +5 to +13, at the time of southern CMB generation.
341 We therefore assign this crustal endmember an average εHf of +8 and a Hf concentration averaged
342 from values reported in Lassiter et al., 1995 (2.9 ppm). The Hf isotopic character of Alexander
343 terrane is heterogeneous; most igneous and metaigneous basement is relatively primitive ($\varepsilon Hf_{(t)}$ =
344 +5 to +15), whereas metasedimentary rocks of the Banks Island assemblage, which is thought to
345 be correlative with the northern Alexander terrane, yields zircons with $\varepsilon Hf_{(t)}$ ranging from +12 to

-30 (Tochilin et al., 2014). Given that the quartz-rich metasedimentary units that yield evolved values are volumetrically less significant, we assign an $\varepsilon Hf_{(t)}$ of 0 for Alexander. Hf concentration for Alexander is estimated to be intermediate between mafic rocks of Alexander reported by Israel et al. (2014) (1.8 ppm) and the average of siliciclastic sedimentary rocks reported by McLennan (2001) (5.5 ppm). The $\delta^{18}O$ of Alexander is taken to be +11 ‰, slightly higher than that of Wrangellia-Stikine, because although Alexander basement is not significantly different, there is greater potential involvement of supracrustal rocks. The primitive end-member is assigned an $\varepsilon Hf_{(t)}$ of +13.6 and a Hf concentration of 1.3, which are the values measured from the most mafic rock analyzed in our batholith dataset (sample 15KN38B; SiO_2 = 51%). We assume a mantle-like $\delta^{18}O$ for this end-member (+5.3 ‰; Valley et al., 2005).

Results of Hf-O models show the majority of southern CMB samples forming a tight cluster in Hf-O space near depleted mantle, and do not reveal mixing trends between mantle and any of the likely crustal sources investigated (Fig. 8). There are four samples, however, which have grains recording non-mantle-like $\delta^{18}O$ values, indicating that these samples involve melting of material that had a near-surface history. Two of these samples are Jurassic plutons discussed previously, which also yielded some of the most evolved zircon $\varepsilon Hf_{(t)}$ values recorded in this part of the batholith (average $\varepsilon Hf_{(t)}$ of +8.4 and +8.6). A third, however, yielded zircons with narrowly distributed $\delta^{18}O$ slightly above mantle values (6.2 to 6.4 ‰) and this pluton has a crystallization age of 138 Ma, a time during which there is a pronounced magmatic lull recorded along much of the North American Cordilleran margin (Gehrels et al., 2009; Paterson and Ducea, 2015; Kirsch et al., 2016; Beranek et al., 2017; Cecil et al., 2018). The fourth anomalous sample – a 108 Ma granodiorite collected from our eastern-most field location – yielded uniformly low $\delta^{18}O$ values (4.2 to 4.7 ‰), just below the accepted mantle range. We interpret these results as indicating

variable contamination of mantle-derived melts by heterogeneous supracrustal sources. That these contaminated samples have few commonalities (they range in age from 96 to 153 Ma, are from plutons emplaced during flare-ups and lulls, and are spatially and compositionally diverse) suggests that there is no systematic process controlling the limited isotopic variability in the southern CMB.

The lack of mixing trajectories in our data makes it difficult to identify any of the crustal end-members as possible melt components, even in the slightly contaminated samples (Fig. 8). Overall, the relatively low $\delta^{18}O$ and juvenile $\varepsilon Hf_{(t)}$ nature of southern CMB samples precludes the involvement of > ~ 10% upper crustal materials into any components of the southern batholith. The isotope data, however, are compatible with sourcing from mafic underplates and / or deep crustal materials, which would not have exchanged with $\delta^{18}O$-enriched surface fluids, but, in the case of young arc-related terranes, would have juvenile εHf characteristics. Indeed, it is hard to explain the generation of a large and compositionally diverse batholith from direct melting of mantle sources. Partial melts of depleted mantle ponding in the lower crust and incorporating deep, previously-generated arc rocks and / or the lower crust of Stikine and / or Wrangellia terrane could produce the isotopic and geochemical signatures observed in the southern CMB. As recently described in Collins et al. (2020), cooling and fractionation of basaltic magmas in the lithospheric mantle can also cause water to exsolve, leading to flux-melting of preexisting mafic underplates. This process allows for the generation of large volumes of silicic, isotopically primitive melt in arc systems, much like what is preserved in the southern CMB.

Drivers of flare-ups in the southern Coast Mountains batholith

Arc flare-ups likely occur as the result of increased melt fertility driven by: 1) the introduction of volatiles or different rock compositions into the sub-arc, or 2) changes in temperature or pressure conditions in the mantle wedge or upper plate lithosphere. One model for the former that has received a lot of attention calls on shortening in the rear-arc leading to periodic underthrusting of older, more evolved upper plate materials (Ducea, 2001; Ducea and Barton, 2007; DeCelles et al., 2009; DeCelles and Graham, 2015). In this orogenic cyclicity model, the introduction of hydrous retro-arc crust into the sub-arc melt generation zone ignites flare-ups. Because crust that is inboard of the arc tends to be older, flare-ups in other arcs, such as the Sierra Nevada, are characterized by isotopic "pull-downs", so called because igneous rocks generated during these times record lower εNd values (Ducea and Barton, 2007; DeCelles et al., 2009). Although not documented in the Sierra Nevada or other Cordilleran arcs, zircon εHf values should record similar pull-downs during flare-ups because of the strong positive correlation between Nd and Hf isotopes in the terrestrial array (Vervoort and Blichert-Toft, 1999). Periodic flare-ups and associated isotopic pull-downs are generally seen as an internal, autocyclic process. In contrast, an episodic change in mantle melt productivity could also lead to episodicity in arc magmatism, but potentially without the concomitant isotopic pull-down. Indeed, high-flux magmatic episodes without excursions to more crust-like isotopic signatures have recently been recognized in the Sierra Nevada and other continental arcs (Decker et al., 2017; Martínez Ardila et al., 2018; Attia et al., 2020; Klein et al., 2020).

In the southern CMB, isotopic pull-downs in zircon Hf data are ambiguous at best and, together with the O isotope data, preclude the significant involvement of supracrustal materials or old (Precambrian), Hf isotope-depleted crust. These data argue against flare-ups occurring in response to an internal underthrusting model wherein the periodic introduction of older, melt-

414 fertile crust from the rear-arc drives high-flux events. Interestingly, however, whole rock and
415 zircon trace element data indicate that flare-ups may be temporally associated with periods of
416 crustal thickening. Evidence for crustal thickening is seen in elevated whole rock Sr/Y and La/Yb
417 ratios (Fig. 4) and in lower Yb and Ti in zircon (Fig. 7C) during flare-ups. Although high Sr/Y and
418 La/Yb ratios are not unique, surveys of those ratios in modern arcs show that Sr/Y and La/Yb are
419 positively correlated with crustal thickness (Chiaradia, 2015; Profeta et al., 2015). Increases in
420 these chemical indices have been linked to crustal thickening in several arc systems and are being
421 increasingly used as proxies for paleo-thickness (e.g. Kay and Mpodozis, 2001; Schwartz et al.,
422 2011; Chapman et al., 2015). Lower Yb and Ti in zircon is attributed to garnet and/or amphibole
423 fractionation during zircon crystallization, which may indicate increased crustal thickness given
424 the sensitivity of garnet stability to pressure-temperature conditions (Grimes et al., 2015).
425 Taken together, these geochemical trends suggest that the arc crust thickens and the depth
426 of differentiation of batholithic melts increases during flare-up events. Periodic crustal thickening
427 in the southern CMB could result from relamination of subducted buoyant material (Hacker et al.,
428 2011), shortening and imbrication of the forearc (Sauer et al., 2017), or intra-arc shortening and
429 magmatism (Jagoutz and Schmidt, 2013), as recently documented in a similar study in the North
430 Cascades (Shea et al., 2018). As previously discussed, it likely does not result from underthrusting
431 of old, supracrustal materials from the retroarc. Imbrication of supracrustal forearc materials is
432 equally unlikely given that the observed mantle-like $\delta^{18}O$ signatures preclude the melting of near-
433 surface rocks. Periodic relamination of more felsic crustal components removed by subduction
434 erosion is a possible mechanism that could explain the arc thickening and differentiation trends
435 observed during flare-ups (Fig. 4). Intra-arc shortening is also a viable option and is supported in
436 part by documented garnet growth and increasing pressure and temperature during the most

volumetric flare-up at ca. 78 Ma (Bollen et al., *in review*). Similar P-T increases in metamorphic host rocks are not recognized for other flare-ups, however, suggesting that additional mechanisms, such as magmatic underplating, are required.

In addition to temporal changes in chemical signatures suggestive of crustal thickening, the southern CMB also records complex shifts in the loci of magmatism through time. It has been observed that plutons are generally younger in the eastern CMB, indicating an overall progressive inboard migration of magmatism through time (Friedman et al., 1995; Gehrels et al., 2009; Cecil et al., 2018). Greater detail provided by our dense geochronologic coverage in the southern CMB, however, reveals a more complex migration pattern in synch with geochemical variations in magmas. Three notable features of these data are: 1) The inboard advance of the leading edge of the arc (shown in the red dashed line on Fig. 9) appears punctuated; 2) landward advance and trenchward retreat of the arc roughly coincide with the timing of flare-ups and lulls, respectively; 3) the active magmatic footprint of the arc appears to widen during flare-ups and narrow during lulls, as illustrated by the horizontal bars in Fig. 9. For example, plutons emplaced during the Jurassic flare-up (161 – 148 Ma) occupy nearly 120 km of arc width, whereas those emplaced during an ensuing lull at ca. 148 – 130 Ma are found in a < 50 km arc-perpendicular swath.

We note that in the central batholith, spatial changes in the arc in the Jurassic to early Cretaceous are difficult to interpret. This is due to the fact that intrusions emplaced during that time likely reflect two distinct arcs: a western arc, emplaced into Alexander-Wrangellia terrane, with no magmatic activity at ca. 140 – 120 Ma, juxtaposed against an eastern arc, emplaced into Stikine and other related inboard terranes, with continuous early Cretaceous magmatism (Gehrels et al., 2009). In contrast to the central CMB, we suggest that Jurassic – early Cretaceous magmatism to the south represents the southern continuation of the eastern arc based on the

observations that: 1) early Cretaceous magmatism is continuous; 2) magmatism appears to sweep inboard, then outboard, as it does in the eastern arc to the north; and 3) Jurassic – early Cretaceous magmas likely intrude rocks of the Intermontane Superterrane (Rusmore et al., 2013). Dextral displacements within the batholith, such as those proposed in Rusmore et al. (2013), would be parallel to batholithic trends and would only affect post – 85 Ma intrusions (Rusmore et al., 2019). We therefore interpret the spatial record of pluton emplacement as a single arc system that is advancing and / or widening with respect to the trench. As in the case of the Jurassic event, similar landward advances of the arc are recognized during the mid-Cretaceous (ca. 110 Ma) and Late Cretaceous (ca. 78 Ma) magmatic flare-ups (Fig. 9). Post-75 Ma spatial patterns in the southern CMB are less well-defined, but it's possible that a similar advance accompanies the Paleogene (ca. 58 Ma) flare-up. We lack the data density necessary during any of these episodes to evaluate more detailed focusing or other spatial trends, as documented by Ardill et al. (2018) for the central Sierra Nevada.

Although a single mechanism is not required to explain each magmatic event, similarities in migratory patterns and arc geochemical signatures (depletions in heavy REEs) indicate that a similar process is periodically recurring in the arc and driving flare-ups. It is possible that punctuated inboard advance of the arc could enhance the mantle-dominated magmatism observed. As the southern CMB advanced landward, it likely tapped into less depleted, more melt-fertile parts of the continental lithosphere, triggering flare-ups (Fig. 10A). This is attributable to more landward parts of the lithosphere 1) not having been previously melted, and / or 2) having been hydrated and (re)fertilized via the accumulation of metasomatic products from prior flux melting in the main arc, and / or 3) having been (re)fertilized via the underthrusting of older and more cratonic (igneous and quartzofeldspathic) inboard lithosphere (Chapman and Ducea, 2019). As

483 previously discussed, the latter is likely of limited importance in the southern CMB, based on the
484 primitive isotopic signatures observed.

485 Of course this leaves unanswered the question of what causes arc migration to begin with.
486 One possibility is that inboard migration is brought on by temporal variations in orthogonal
487 convergence rate. An increase in convergence rate, if associated with increased plate coupling,
488 would not only gradually shift magmatism inboard and but could also lead to tectonic thickening
489 in the arc and the increased bulk rock Sr/Y and $La/Yb_{(N)}$ ratios observed. Thickening could be
490 enhanced by the addition of voluminous mafic underplates during the flare-up event. Increased
491 convergence and plate coupling, if accompanied by a decrease in slab dip, could also explain a
492 widening of the arc footprint. Orthogonal convergence rates for the Coast Mountain batholith
493 region, as presented in Kirsch et al. (2016), vary considerably throughout the ca. 150 m.y. lifespan
494 of the arc, from slightly negative (divergent) values early in the early arc (pre-160 Ma) to almost
495 200 mm/yr in Cretaceous time. Although the temporal variability is highly complex, increases in
496 convergence rate broadly coincide with all but the most recent (ca. 58 Ma) flare-up in the southern
497 CMB. One problem with this mechanism is that magmatic tempo in the CMB appears to change
498 along strike, which would require spatially variable convergence rates at unlikely scales (~ 150
499 km of arc length) (Cecil et al., 2018).

500 Another possibility is that arc migration is driven by non-steady-state forearc subduction
501 erosion, as proposed in Jicha and Kay (2018). In this scenario, the periodic erosion of forearc crust
502 drives the arc system landward, though the trench-arc distance remains the same. Relamination of
503 forearc crustal components, particularly if they are of the mafic, isotopically Wrangellia terrane,
504 could promote crustal thickening and supply source rock to the subarc melt zone that is compatible
505 with the isotopic signatures observed in southern CMB magmas. This scenario has the advantage

506 of allowing for more along-strike variability in magmatic patterns, but is difficult to evaluate given
507 that much of the forearc to the CMB is not exposed. In either case, coeval arc advance and
508 magmatic flare-ups are observed and are linked to crustal thickening, trends which have been
509 documented in other Cordilleran arcs (Haschke et al., 2002; Karlstrom et al., 2014).

510 Eventually, flare-ups in the southern CMB wane, perhaps as fertile mantle depletes, or as
511 the arc lithosphere overthickens, impinging on the subducting slab and cutting off asthenospheric
512 circulation in the mantle wedge (Chin et al., 2012; Karlstrom et al., 2014), or as the hot mantle
513 wedge is pinched out by slab flattening, which Haschke et al. (2002) argues leads to magmatic
514 gaps in the Andean arc record. These waning stages appear to coincide with lower and more
515 homogeneous bulk rock Sr/Y and $La/Yb_{(N)}$ (Fig. 4) and with trenchward retreat of the arc (Fig. 9).
516 We speculate that these features result from the periodic removal of dense arc residue, which
517 pushes the arc back, aligning it with thinned and / or depleted arc lithosphere (Fig. 10B). During
518 this time, the arc enters a lull phase and the depth of magmatic differentiation decreases. A return
519 to normal supra-slab mantle convection and landward migration of the arc into be more fertile
520 lithosphere is required to start the next flare-up cycle.

521

522 CONCLUSIONS

523 New zircon Hf and O isotopic data from Jurassic to Eocene plutons of the southern Coast
524 Mountains batholith (CMB) reveal mantle-dominated melt sources across a broad swath of the arc
525 and over ~ 120 m.y. of episodic arc activity. This suggests that magmatic episodicity is not driven
526 by the periodic input of evolved, supracrustal materials in sub-arc melt zones, but rather must be
527 associated with spatiotemporal changes in mantle melt productivity. Our results support recent
528 work that documents the significance of mantle melt contributions to continental batholiths

(Decker et al., 2017; Martinez Ardila, 2019; Attia et al., 2020; Klein et al., 2020). This has important implications for the generation of continental crust in arc systems and implies significant new addition, and limited recycling, of crust along plate margins. Geochemical indices such as whole rock Sr/Y and La/Yb, and zircon Ti and Yb concentrations change as a function of magmatic flux, suggesting that although the mantle remains the dominant melt source, the thickness of arc lithosphere increases during flare-ups and decreases during lulls. A closer look at spatial trends in the available geochronology for the southern CMB reveals periods of inboard arc advance and retreat, leading us to suggest that arc migratory trends fundamentally control magmatic tempo. In our preferred model, the arc migrates inboard, accessing previously (re)hydrated and (re)fertilized lithosphere, triggering mantle-like magmatic flare-ups, as proposed in Chapman and Ducea (2019). These inboard arc advances are accompanied by tectonic and magmatic thickening of the arc. Eventually, dense arc residue formed at the base of the arc column becomes gravitationally unstable and is convectively removed, forcing the trenchward retreat of the arc into regions where the sub-arc mantle lithosphere is absent or depleted. Such a shift produces lower volumes of melt, and magmas with geochemical signatures consistent with generation and emplacement in tectonically thinned lithosphere. Overall, the results of this study highlight the fact that the growth of large volume Cordilleran batholiths does not require significant recycling of preexisting crust, and that magmatic tempos can be highly episodic if the mantle is temporally and spatially heterogeneous in terms of its degree of hydration and melt fertility.

ACKNOWLEDGMENTS

This research was supported by National Science Foundation awards EAR-1347219 and EAR-1655152 to Cecil, EAR-1347375 to Gehrels, EAR-1347212 to Rusmore, EAR-1347341 to

552 Stowell, and EAR-1338583 for support of the Arizona LaserChron Center. WiscSIMS is supported
553 by the U.S. National Science Foundation (EAR-1658823) and the University of Wisconsin-
554 Madison. The authors are grateful for insightful reviews by Scott Paterson and Jonathan Miller,
555 which greatly improved the paper. They also gratefully acknowledge Mark Pecha and Nicky
556 Geisler for their help in acquiring the zircon Hf and trace element data, and Kyle Oye and Christine
557 Truong for their help with whole rock geochemical analyses. Don Willson of Silver King Ventures
558 and Mike King and Jim Henderson of White Saddle Air Services provided critical field logistical
559 support.

560

561 REFERENCES

562 Alberts, D., Gehrels, G., and Nelson, J, 2021, U-Pb and Hf isotopic analysis of detrital zircons
563 from Paleozoic and Cretaceous strata of southern Vancouver Island, British Columbia;
564 Lithosphere, v. 2021, 20 p., doi: 10.2113/2021/7866944.
565 Ardill, K., Paterson, S., and Memeti, V., 2018, Spatiotemporal magmatic focusing in upper-mid
566 crustal plutons of the Sierra Nevada arc: Earth and Planetary Science Letters, v. 498, p.
567 88-100, doi: 10.1016/j.epsl.2018.06.023.
568 Armstrong, R. L., 1988, Mesozoic and Cenozoic magmatic evolution of the Canadian Cordillera,
569 *in* Clark, S. P., Burchfiel, B. C., and Suppe, J., eds., Processes in continental lithospheric
570 deformation, Geological Society of America Special Paper 218, p. 55-91.
571 Attia, S., Cottle, J.M., and Paterson, S.R., 2020, Erupted zircon record of continental crust
572 formation during mantle driven arc flare-ups: Geology, v. 48, no. 5, p. 446-451, doi:
573 10.1130/g46991.1.
574 Bahlburg, H., Vervoort, J. D., DuFrane, S. A., Carlotto, V., Reimann, C., and Cardenas, J., 2011,
575 The U-Pb and Hf isotope evidence of detrital zircons of the Ordovician Ollantaytambo
576 Formation, southern Peru, and the Ordovician provenance and paleogeography of
577 southern Peru and northern Bolivia: Journal of South American Earth Sciences, v. 32, no.
578 3, p. 196-209, doi: 10.1016/j.sames.2011.07.002.
579 Barresi, T., Nelson, J. L., and Friedman, R., 2015, Evolution of the Hazelton arc near Terrace,
580 British Columbia: Stratigraphic, geochronological, and geochemical constraints on a Late
581 Jurassic - Early Jurassic arc and Cu-Au porphyry belt: Canadian Journal of Earth
582 Sciences, v. 52, p. 466-494, doi: 10.1139/cjes-2014-0155.
583 Beranek, L. P., McClelland, W. C., van Staal, C. R., Israel, S., and Gordee, S. M., 2017, Late
584 Jurassic flare-up of the Coast Mountains arc system, NW Canada, and dynamic linkages
585 across the northern Cordilleran orogen: Tectonics, v. 36, no. 5, p. 877-901, doi:
586 10.1002/2016tc004254.

587 Bollen, E. M., Stowell, H. H., Rusmore, M. E., Woodsworth, G. J., and Cecil, M. R., *in review*,
588 The tempo of metamorphism and magmatism, Coast Mountains batholith, Canada:
589 Journal of Metamorphic Geology.
590 Brandon, M. T., Orchard, M. J., Parrish, R. R., Sutherland Brown, A., and Yorath, C. J., 1986,
591 Fossil ages and isotopic dates from the Paleozoic Sicker Group and associated intrusive
592 rocks, Vancouver Island, British Columbia: Geological Survey of Canada Paper 86-1A,
593 p. 683-696.
594 Castillo, P. R., 2012, Adakite petrogenesis: Lithos, v. 134-135, p. 304-316, doi:
595 10.1016/j.lithos.2011.09.013.
596 Cecil, M. R., Gehrels, G., Ducea, M. N., and Patchett, P. J., 2011, U-Pb-Hf characterization of
597 the central Coast Mountains batholith: Implications for petrogenesis and crustal
598 architecture: Lithosphere, v. 3, no. 4, p. 247-260, doi: 10.1130/l134.1.
599 Cecil, M. R., Rotberg, G., Ducea, M. N., Saleeby, J.B., and Gehrels, G.E., 2012, Magmatic
600 growth and batholithic root development in the northern Sierra Nevada, California:
601 Geosphere, v. 8, p.592-606, doi:10.1130/GES00729.1.
602 Cecil, M. R., Rusmore, M. E., Gehrels, G. E., Woodsworth, G. J., Stowell, H. H., Yokelson, I.,
603 Chisom, C., Trautman, M., and Homan, E., 2018, Along-strike variation in the magmatic
604 tempo of the Coast Mountains batholith, British Columbia, and implications for processes
605 controlling episodicity in arcs: Geochemistry, Geophysics, Geosystems, v. 19, doi:
606 10.1029/2018GC007874.
607 Chapman, J. B., and Ducea, M. N., 2019, The role of arc migration in Cordilleran orogenic
608 cyclicity: Geology, v. 47, no. 7, p. 627-630, doi: 10.1130/g36996.1.
609 Chapman, J. B., Ducea, M. N., DeCelles, P. G., and Profeta, L., 2015, Tracking changes in
610 crustal thickness during orogenic evolution with Sr/Y: An example from the North
611 American Cordillera: Geology, v. 43, no. 10, p. 919-922, doi: 10.1130/g36996.1.
612 Chapman, J. B., Gehrels, G. E., Ducea, M. N., Giesler, N., and Pullen, A., 2016, A new method
613 for estimating parent rock trace element concentrations from zircon: Chemical Geology,
614 v. 439, p. 59-70, doi: 10.1016/j.chemgeo.2016.06.014.
615 Chiaradia, M., 2015, Crustal thickness control on Sr/Y signatures of recent arc magmas: an Earth
616 scale perspective: Sci Rep, v. 5, p. 8115, doi: 10.1038/srep08115.
617 Chin, E. J., Lee, C. T. A., Luffi, P. I., and Tice, M., 2012, Deep lithospheric thickening and
618 refertilization beneath continental arcs: Case study of the P,T and compositional
619 evolution of peridotite xenoliths from the Sierra Nevada, California: Journal of Petrology,
620 v. 53, no. 3, p. 477-511, doi: 10.1093/petrology/egr069.
621 Collins, W. J., Murphy, J. B., Johnson, T. E., and Huang, H., 2020, Critical role of water in the
622 formation of continental crust: Nature Geoscience, v. 13, p. 331-338. doi:
623 10.1038/s41561-020-0573-6.
624 Dafov, M., Carrera, A., Gehrels, G., Alberts, D., Pereira, M., Cecil, M.R., Rusmore, M.E.,
625 Stowell, H.H., Woodsworth, G.J., 2020, U-Th-Pb Geochronology and Lu-Hf Isotope
626 Geochemistry of Detrital Zircons in Metasedimentary Rocks of the Southern Coast
627 Mountains Batholith: Lithosphere, v.2020, 21 p. doi: 10.2113/2020/8854686.
628 DeBari, S., Anderson, R. G., and Mortensen, J. K., 1999, Correlation among lower to upper
629 crustal components in an island arc: The Jurassic Bonanza arc, Vancouver Island,
630 Canada: Canadian Journal of Earth Sciences, v. 36, p. 1371-1413, doi: 10.1139/e99-029.
631 DeCelles, P. G., Ducea, M. N., Kapp, P., and Zandt, G., 2009, Cyclicity in Cordilleran orogenic
632 systems: Nature Geoscience, v. 2, no. 4, p. 251-257, doi: 10.1038/ngeo469.

633 DeCelles, P. G., and Graham, S. A., 2015, Cyclical processes in the North American Cordilleran
634 orogenic system: Geology, v. 43, no. 6, p. 499-502, doi: 10.1130/G36482.1.
635 Decker, M., Schwartz, J.J., Stowell, H.H., Klepeis, K.A., Tulloch, A.J., Kitajima, K., Valley,
636 J.W., and Kylander-Clark, A.R.C., 2017, Slab-Triggered Arc Flare-up in the Cretaceous
637 Median Batholith and the Growth of Lower Arc Crust, Fiordland, New Zealand: Journal
638 of Petrology, v. 58, no. 6, p. 1145-1171, doi: 10.1093/petrology/egx049.
639 de Silva, S.L., Riggs, N.R., Barth, A.P., 2015, Quickening the pulse: Fractal tempos in
640 continental arc magmatism: Elements, v. 11, p. 113-118, doi:
641 10.2113/gselements.11.2.113.
642 Dhuime, B., Hawkesworth, C. J., and Cawood, P. A., 2011, When Continents Formed: Science,
643 v. 331, p. 154-155, doi: 10.1126/science.1201245.
644 Dostal, J., Gale, V., and Church, B. N., 1999, Upper Triassic Takla Group volcanic rocks of
645 Stikine Terrane, north-central British Columbia: geochemistry, petrogenesis, and tectonic
646 implications: Canadian Journal of Earth Sciences, v. 36, p. 1483-1494.
647 Dostal, J., Keppie, J. D., and Ferri, F., 2009, Extrusion of high-pressure Cache Creek rocks into
648 the Triassic Stikinia Quesnellia arc of the Canadian Cordillera: implications for terrane
649 analysis of ancient orogens and palaeogeography: Geological Society, London, Special
650 Publications, v. 327, p. 71-87, doi: 10.1144/SP327.5.
651 Ducea, M. N., 2001, The California arc: Thick granitic batholiths, eclogitic residues,
652 lithospheric-scale thrusting, and magmatic flare-ups: GSA Today, v. 11, no. 11, p. 4-10.
653 Ducea, M., and Barton, M. D., 2007, Igniting flare-up events in Cordilleran arcs: Geology, v. 35,
654 doi: 10.1130/G23898A.1.
655 Frost, B. R., Barnes, C. G., Collins, W. J., Arculus, R. J., Ellis, D. J., and Frost, C. D., 2001, A
656 geochemical classification for granitic rocks: Journal of Petrology, v. 42, no. 11, p. 2033-
657 2048, doi: 10.1093/petrology/42.11.2033.
658 Friedman, R.M., Mahoney, J.B., Cui, Y., 1995, Magmatic evolution of the southern Coast Belt:
659 Constraints from Nd-Sr isotopic systematics and geochronology of the southern Coast
660 Plutonic Complex: Canadian Journal of Earth Sciences, v.32, p.1681-1698, doi:
661 10.1139/e95-133.
662 Gashnig, R. M., Vervoort, J. D., Lewis, R. S., and Tikoff, B., 2011, Isotopic evolution of the
663 Idaho Batholith and Challis Intrusive Complex, northern US Cordillera: Petrology, v. 52,
664 no. 12, p. 2397-2429, doi: 10.1093/petrology/egr050.
665 Gehrels, G. E., and Kapp, P. A., 1998, Detrital zircon geochronology and regional correlation of
666 metasedimentary rocks in the Coast Mountains, southeastern Alaska: Canadian Journal of
667 Earth Sciences, v. 35, p. 269-279.
668 Gehrels, G., and Pecha, M., 2014, Detrital zircon U-Pb geochronology and Hf isotope
669 geochemistry of Paleozoic and Triassic passive margin strata of western North America:
670 Geosphere, v. 10, p. 49-65, doi: 10.1130/GES00889.1.
671 Gehrels, G., Rusmore, M., Woodsworth, G., Crawford, M., Andronicos, C., Hollister, L.,
672 Patchett, J., Ducea, M., Butler, R., Klepeis, K., Davidson, C., Friedman, R., Haggart, J.,
673 Mahoney, B., Crawford, W., Pearson, D., and Girardi, J., 2009, U-Th-Pb geochronology
674 of the Coast Mountains batholith in north-coastal British Columbia: Constraints on age
675 and tectonic evolution: Geological Society of America Bulletin, v. 121, no. 9-10, p. 1341-
676 1361, doi: 10.1130/b26404.1.
677 Girardi, J. D., Patchett, P. J., Ducea, M. N., Gehrels, G. E., Cecil, M. R., Rusmore, M. E.,
678 Woodsworth, G. J., Pearson, D. M., Manthei, C., and Wetmore, P., 2012, Elemental and

679 Isotopic Evidence for Granitoid Genesis From Deep-Seated Sources in the Coast
680 Mountains Batholith, British Columbia: Journal of Petrology, v. 53, no. 7, p. 1505-1536,
681 doi: 10.1093/petrology/egs024.
682 Greene, A. R., Scoates, J. S., Weis, D., Nixon, G. T., and Kieffer, B., 2009, Melting history and
683 magmatic evolution of basalts and picrites from the accreted Wrangellia Oceanic Plateau,
684 Vancouver Island, Canada: Journal of Petrology, v. 50, no. 3, p. 467-505, doi:
685 10.1093/petrology/egp008.
686 Grimes, C. B., Wooden, J. L., Cheadle, M. J., and John, B. E., 2015, "Fingerprinting" tectono-
687 magmatic provenance using trace elements in igneous zircon: Contributions to
688 Mineralogy and Petrology, v. 170, no. 46, doi: 10.1007/s00410-015-1199-3.
689 Hacker, B.R., Kelemen, P.B., and Behn, M.D., 2011, Differentiation of the continental crust by
690 relamination: Earth and Planetary Science Letters, v. 307, no. 3-4, p. 501-516. doi:
691 10.1016/j.epsl.2011.05.024.
692 Haschke, M., Siebel, W., Gunther, A., and Scheuber, E., 2002, Repeated crustal thickening and
693 recycling during the Andean orogeny in north Chile (21 ° - 26 °S): Journal of
694 Geophysical Research, v. 107, p. ECV 6-1 - 6-18. doi: 10.1029/2001JB000328.
695 Hollister, L.S.., Andronicos, C.L., 2006, Formation of new continental crust in Western British
696 Columbia during transpression and transtension: Earth and Planetary Science Letters, v.
697 249, p. 28-38. doi: 10.1016/j.epsl.2006.06.042.
698 Israel, S., Beranek, L., Friedman, R.M., and Crowley, J.L., 2014, New ties between the
699 Alexander terrane and Wrangellia and implications for North America Cordilleran
700 evolution: Lithosphere, v. 6, no. 4, p. 270-276, doi: 10.1130/l364.1.
701 Jackson, J. L., Gehrels, G. E., Patchett, J., and Mihalynuk, M. G., 1991, Stratigraphic and
702 isotopic link between the northern Stikine terrane and an ancient continental margin
703 assemblage, Canadian Cordillera: Geology, v. 19, p. 1177-1180.
704 Jagoutz, O., and Schmidt, M.W., 2013, The composition of the foundered complement to the
705 continental crust and a re-evaluation of fluxes in arcs: Earth and Planetary Science
706 Letters, v. 371, p. 177-190. doi: 10.1016/j.epsl.2013.03.051.
707 Jicha, B.R. and Kay, S.M., 2018, Quantifying arc migration and the role of forearc subduction
708 erosion in the Central Aleutians: Journal of Volcanology and Geothermal Research, v.
709 360, p. 84-99. doi: 10.1016/j.volgeores.2018.06.016.
710 Karlstrom, L., Lee, C.-T. A., and Manga, M., 2014, The role of magmatically driven lithospheric
711 thickening on arc front migration: Geochemistry, Geophysics, Geosystems, v. 15, p.
712 2655-2675. doi: 10.1002/2014GC005355.
713 Kay, S. M., and Mpodozis, C., 2001, Central Andean ore deposits linked to evolving shallow
714 subduction systems and thickening crust: GSA Today, v. 11, no. 3, p. 4-9, doi:
715 10.1130/1052-5173(2001)011<0004:CAODLT>2.0.CO;2.
716 King, E. M., and Valley, J. W., 2001, The source, magmatic contamination, and alteration of the
717 Idaho batholith: Contributions to Mineralogy and Petrology, v. 142, p. 72-88, doi:
718 10.1007/s004100100278.
719 Kirsch, M., Paterson, S.R., Wobbe, F., Ardila, A.M.M., Clausen, B.L., and Alasino, P.H., 2016,
720 Temporal histories of Cordilleran continental arcs: Testing models for magmatic
721 episodicity: American Mineralogist, v. 101, no. 9-10, p. 2133-2154, doi: 10.2138/am-
722 2016-5718.

Kita, N. T., Ushikubo, T., and Valley, J. W., 2009, High precision SIMS oxygen isotope analysis and the effect of sample topography: Chemical Geology, v. 264, no. 1-4, p. 43-57, doi: 10.1016/j.chemgeo.2009.02.012.

Kistler, R. W., Wooden, J. L., Premo, W. R., and Morton, D. M., 2014, Pb-Sr-Nd-O isotopic characterization of Mesozoic rocks throughout the northern end of the Peninsular Ranges batholith: Isotopic evidence for the magmatic evolution of oceanic arc-continental margin accretion during the Late Cretaceous of southern California, *in* Morton, D. M., and Miller, F. K., eds., Peninsular Ranges Batholith, Baja California and Southern California, Geological Society of America Memoir 211, p. 263-316, doi: 10.1130/2014.1211(07).

Klein, B.Z., Jagoutz, O., and Ramezani, J., 2021, High-precision geochronology requires that ultrafast mantle-derived magmatic fluxes built the transcrustal Bear Valley Intrusive Suite, Sierra Nevada, California, USA: Geology, v. 49, no. 1, p. 106-110, doi: 10.1130/g47952.1.

Lackey, J. S., Valley, J. W., Chen, J. H., and Stockli, D. F., 2008, Dynamic Magma Systems, Crustal Recycling, and Alteration in the Central Sierra Nevada Batholith: The Oxygen Isotope Record. Journal of Petrology, v. 49, p. 1397-1426, doi:10.1093/petrology/egn030.

Lackey, J. S., Cecil, M. R., Windham, C. J., Frazer, R. E., Bindeman, I. N., and Gehrels, G. E., 2012, The Fine Gold Intrusive Suite: The roles of basement terranes and magma source development in the Early Cretaceous Sierra Nevada batholith: Geosphere, v. 8, no. 2, p. 292-313, doi: 10.1130/ges00745.1.

Madsen, J. K., Thorkelson, D. J., Friedman, R., and Marshall, D. D., 2006, Cenozoic to recent plate configurations in the Pacific Basin: Ridge subduction and slab window magmatism in western North America: Geosphere, v. 2, no. 1, p. 11-34. Doi: 10.1130/GES00020.1.

Martínez Ardila, A.M., Paterson, S.R., Memeti, V., Parada, M.A., and Molina, P.G., 2019, Mantle driven cretaceous flare-ups in Cordilleran arcs: Lithos, v. 326, p. 19-27, doi: 10.1016/j.lithos.2018.12.007.

Massey, N. W. D., and Friday, S. J., 1989, Geology of the Alberni-Nanaimo Lakes area, Vancouver Island, *in* Geological Fieldwork, British Columbia Ministry of Energy, Mines and Petroleum Resources, Geological Survey Branch, Paper 1989-1, p. 61-74.

McLennan, S.M., 2001, Relationships between the trace element composition of sedimentary rocks and upper continental crust: Geochemistry Geophysics Geosystems, v. 2, doi: 10.1029/2000gc000109.

Monger, J. W. H., Price, R. A., and Tempelman-Kluit, D. J., 1982, Tectonic accretion and the origin of the two major metamorphic and plutonic welts in the Canadian Cordillera: Geology, v. 10, p. 70-75. doi: 10.1130/0091-7613(1982)10<70:TAATOO>2.0.CO;2.

Nelson, J., 1979, The western margin of the Coast plutonic complex on Hardwicke and West Thurlow Islands, British Columbia: Canadian Journal of Earth Sciences, v. 16, no. 6, p. 1166-1175. doi: 10.1139/e79-103.

Nelson, J. L., Colpron, M., Piercey, S. J., Dusel-Bacon, C., Murphy, D. C., and Roots, C., 2006, Paleozoic tectonic and metallogenetic evolution of pericratonic terranes in Yukon, northern British Columbia and eastern Alaska, *in* Colpron, M., and Nelson, J. L., eds., Paleozoic Evolution and Metallogeny of Pericratonic Terranes at the Ancient Pacific Margin of North America, Canadian and Alaskan Cordillera, Geological Association of Canada Special Paper 45, p. 323-360.

Paterson, S. R., and Ducea, M. N., 2015, Arc Magmatic Tempos: Gathering the Evidence: Elements, v. 11, no. 2, p. 91-98, doi: 10.2113/gselements.11.2.91.

769 Profeta, L., Ducea, M. N., Chapman, J. B., Paterson, S. R., Gonzales, S. M. H., Kirsch, M.,
770 Petrescu, L., and DeCelles, P. G., 2015, Quantifying crustal thickness over time in
771 magmatic arcs: Scientific Reports, v. 5, doi: 10.1038/srep17786.
772 Ruks, T. W., 2015, Stratigraphic and paleotectonic studies of Paleozoic Wrangellia and its
773 contained volcanogenic massive sulfide occurrences, Vancouver Island, British
774 Columbia, Canada [PhD: University of British Columbia], doi: 10.14288/1.0166640.
775 Rusmore, M. E., Bogue, S. W., and Woodsworth, G. J., 2013, Paleogeography of the Insular and
776 Intermontane terranes reconsidered: Evidence from the southern Coast Mountains
777 Batholith, British Columbia: Lithosphere, v. 5, no. 5, p. 521-536, doi: 10.1130/l288.1.
778 Rusmore, M. E., Woodsworth, G. J., Cecil, M. R., Bollen, E. M., Stowell, H. H., Gehrels, G. E.,
779 and Grove, M. J., 2019, Newly recognized Latest Cretaceous transcurrent faulting within
780 the Coast Mountains batholith (CMB), British Columbia: Geological Society of America
781 *Abstracts with Programs*, v. 51, no. 4, doi: 10.1130/abs/2019CD-329318.
782 Samson, S. D., Patchett, P. J., McClelland, W. C., and Gehrels, G. E., 1991, Nd and Sr isotopic
783 constraints on the petrogenesis of the west side of the northern Coast Mountains
784 batholith, Alaskan and Canadian Cordillera: Canadian Journal of Earth Sciences, v. 28,
785 no. 6, p. 939-946, doi: 10.1139/e91-085.
786 Sauer, K.B., Gordon, S.M., Miller, R.B., Vervoort, J.D., and Fisher, C.M., 2017, Transfer of
787 Metasupracrustal Rocks to Midcrustal Depths in the North Cascades Continental
788 Magmatic Arc, Skagit Gneiss Complex, Washington: Tectonics, v. 36, no. 12, p. 3254-
789 3276. Doi: 10.1016/j.epsl.2013.03.051.
790 Schwartz, J. J., Johnson, K., Miranda, E. A., and Wooden, J. L., 2011, The generation of high
791 Sr/Y plutons following Late Jurassic arc-arc collision in the Blue Mountains province,
792 NE Oregon: Lithos, v. 126, p. 22-41, doi: 10.1016/j.lithos.2011.05.005.
793 Shea, E.K., Miller, J.S., Miller, R.B., Chan, C.F., Kent, A.J.R., Hancher, J.M., Dustin, K., and
794 Elkins, S., 2018, Time scale for the development of thickened crust in the Cretaceous
795 North Cascades magmatic arc, Washington, and relationship to Cretaceous flare-up
796 magmatism: Lithosphere, v. 10, no. 6, p. 708-722, doi: 10.1130/l1001.1.
797 Stock, J., and Molnar, P., 1988, Uncertainties and implications of the Late Cretaceous and
798 Tertiary position of North America relative to the Farallon, Kula and Pacific plates:
799 Tectonics, v. 7, p. 1339-1384.
800 Sundell, K. E., Saylor, J. E., and Pecha, M., 2019, Sediment provenance and recycling of detrital
801 zircons from Cenozoic Altiplano strata in southern Peru and implications for the crustal
802 evolution of west-central South America, *in* Horton, B. K., and Folguera, A., eds.,
803 Andean Tectonics, p. 363-397, doi: 10.1016/B978-0-12-816009-1.00014-9.
804 Tochilin, C. J., Gehrels, G. E., Nelson, J., and Mahoney, J. B., 2014, U-Pb and Hf isotope
805 analysis of detrital zircons from the Banks Island assemblage (coastal British Columbia)
806 and southern Alexander terrane (southeast Alaska): Lithosphere, v. 6, no. 3, p. 200-215,
807 doi: 10.1130/l338.1.
808 Valley, J. W., 2003, Oxygen Isotopes in Zircon: Reviews in Mineralogy and Geochemistry, v 53,
809 p. 343-385. doi: 10.2113/0530343.
810 Valley, J. W. and Kita, N. T., 2009, *In situ* Oxygen Isotope Geochemistry by Ion Microprobe, In:
811 Fayek M. (ed) MAC Short Course: Secondary Ion Mass Spectrometry in the Earth
812 Sciences, v 41, p. 19-63.
813 Valley, J. W., Lackey, J. S., Cavosie, A. J., Clechenko, C. C., Spicuzza, M. J., Basei, M. A. S.,
814 Bindeman, I. N., Ferreira, V. P., Sial, A. N., King, E. M., Peck, W. H., Sinha, A. K., and

Wei, C. S., 2005, 4.4 billion years of crustal maturation: oxygen isotope ratios of magmatic zircon: Contributions to Mineralogy and Petrology, v. 150, p. 561-580, doi: 10.1007/s00410-005-0025-8.

Vervoort, J. D., and Blichert-Toft, J., 1999, Evolution of the depleted mantle: Hf isotope evidence from juvenile rocks through time: Geochimica et Cosmochimica Acta, v. 63, no. 3-4, p. 533-556.

Wang, X.-L., Coble, M. A., Valley, J. W., Shu, X.-J., Kitajima, K., Spicuzza, M. J., and Sun, T., 2014, Influence of radiation damage on late Jurassic zircon from southern China: Evidence from in situ measurement of oxygen isotopes, laser Raman, U-Pb ages, and trace elements. Chemical Geology, v. 389, p. 122-136.

Wetmore, P. H., and Ducea, M. N., 2011, Geochemical evidence of a near-surface history for source rocks of the central Coast Mountains Batholith, British Columbia: International Geology Review, v. 53, no. 2, p. 230-260, doi: 10.1080/00206810903028219.

Wheeler, J. O., and McFeely, P., 1991, Tectonic assemblage map of the Canadian Cordillera and adjacent parts of the United States of America: Geological Survey of Canada Map 1713, scale 1:2,000,000.

Wiedenbeck, M., Hanchar, J. M., Peck, W. H., Sylvester, P., and Valley, J. W., 2004, Further characterization of the 91500 zircon crystal: Geostandards and Geoanalytical Research, v. 28, p. 9-39, doi: 10.1111/j.1751-908X.2004.tb01041.x.

Yorath, C. J., Sutherland Brown, A., and Massey, N. W. D., 1999, LITHOPROBE, southern Vancouver Island, British Columbia: geology: Geological Survey of Canada, Bulletin 498, 145 p.

FIGURE CAPTIONS

Figure 1. Simplified geologic map of the Bute Inlet – Knight Inlet – Mt. Waddington region of the southern Coast Mountains batholith, British Columbia. All sampling locations are shown and symbolized according to the analyses performed at each location. Color-coded age information is from Cecil et al., 2018.

Figure 2. Cathodoluminescence (CL) images (A), U-Pb ages (B) and initial εHf values for a representative sample of the southern Coast Mountains batholith (sample 15KS79 from Knight Inlet). The CL images show large, uncomplicated zircon grains with characteristic oscillatory or sector zoning, consistent with new igneous growth. Measured U-Pb ages and initial εHf values are

849 relatively invariant between grains within a given sample, as reflected in small standard deviations
850 of the weighted means and MSWD values close to 1.
851
852 Figure 3. Whole-rock major element data showing the geochemical characteristics of the southern
853 CMB. A: Total alkali silica diagram showing range in pluton compositions as a function of age.
854 Flare-up and lull age groups are based on the timing of magmatic flux events, as reported in Cecil
855 et al., 2018. Intrusive rocks of the southern batholith are metaluminous to mildly peraluminous
856 (B), calcic to calc-alkalic (C) and magnesian (D). A/CNK in part B is given as
857 $Al_2O/(CaO+K_2O+Na_2O)$ in molar abundance. Southern CMB intrusions are geochemically similar
858 to those of the central batholith (grade shaded polygons; Girardi et al., 2012) and to granitoids
859 from other Cordilleran arc systems (cross-hatched polygons) (Frost et al., 2001).
860
861 Figure 4. Bivariate plots for the southern Coast Mountains batholith showing whole-rock $La/Yb_{(N)}$
862 and Sr/Y ratios, plotted against $Yb_{(N)}$ and Y (ppm) in (A) and (B), respectively. The same ratios,
863 plotted against age, are shown in parts (C) and (D). Inverted triangles in (C) and (D) represent
864 calculated averages for each time period. Partial melting and mineral fractionation trends after
865 Castillo, 2012. Sample symbology is the same as shown in Figure 3. The vertical shaded bars in
866 parts (C) and (D) represent southern CMB flare-up events, as described in Cecil et al., 2018.
867 MORB – mid-ocean ridge basalt; ADR – field representing normal arc andesite, dacite, and
868 rhyolite lavas; amph – amphibole; cpx – clinopyroxene.
869
870 Figure 5. Histograms showing the distributions of all individual zircon εHf (A) and zircon $\delta^{18}O$
871 (B) measurements. Flare-up and lull periods are the same as shown in Figures 3 and 4. The

distribution of zircon εHf from the central Coast Mountains batholith (CMB) is shown for comparison in (A); data from Cecil et al., 2011. Range of mantle zircon $\delta^{18}O$ from Valley et al., 2005.

Figure 6. Plot showing initial zircon εHf values for all analyzed grains (small white circles) in the southern CMB (*N* = number of samples analyzed; *n* = number of zircon grains analyzed). The average uncertainty for individual measurements is shown in the lower right at the 2σ level. Individual grain analyses were contoured, and running mean calculated through them, using the Hafnium Plotter program (Sundell et al., 2019). Larger blue circles represent sample averages. Typical standard deviation of sample averages is <1.5 epsilon units at the 2σ level. Depleted mantle evolution is determined using $^{176}Hf/^{177}Hf_{(0)} = 0.283225$ and $^{176}Lu/^{177}Hf_{(0)} = 0.038512$ (Vervoort and Blichert-Toft, 1999). Dashed lines indicate field of "juvenile" values (0-5 εHf units below DM), after Bahlburg et al., 2011. Gray shaded curve at the bottom of the plot shows magmatic areal addition rate in km^2/m.y. in the southern CMB, from Cecil et al. 2018.

Figure 7. Zircon trace element geochemical plots for intrusive rocks of the southern CMB. Chondrite-normalized spider diagrams of REE compositions for time period averages are shown in (A). Bivariate plots of U/Yb vs Hf (B) and Ti vs Yb (C) are shown with the compilation of continental arc data from Grimes et al., 2015.

Figure 8. Binary mixture modeling showing sample-averaged zircon Hf and O isotope data from southern CMB intrusions. Sample symbols are the same as in figure 3. The majority of analyzed samples form a tight cluster with values near the depleted end of the mantle array. The average

895 $\delta^{18}O$ value for the sample with an asterisk does not include a single grain with a measured value
896 of 8.3 ‰ (gray diamond). WT – Wrangellia terrane; ST – Stikine terrane; AT – Alexander terrane;
897 YTT – Yukon-Tanana terrane. See text for discussion of endmember isotopic compositions.
898
899 Figure 9. Plot of pluton U-Pb ages as a function of distance from the coastline for the southern
900 CMB. Colors are the same as in Figure 1. Also shown is the magmatic areal addition rate for the
901 southern batholith in km^2/m.y. (gray curve). Each blue bar represents the width of the arc during
902 5 m.y. intervals, based on pluton geochronology from Cecil et al., 2018. The red dashed line
903 outlines the leading edge of magmatism though time and, together with the black arrows,
904 represents the interpreted temporal pattern of arc advance and retreat discussed in the text.
905
906 Figure 10. Schematic cross-sections showing the potential role of arc migration in generating
907 mantle-driven flare-ups in the southern CMB, after Chapman and Ducea, 2019. A: Landward
908 migration of the arc into previously (re)fertilized and hydrated mantle lithosphere triggers high
909 flux melting and leads to arc thickening. Basaltic magmas stagnate near the base of the crust, where
910 they cool and fractionate, exsolving water that promotes melting of overlying mafic underplates
911 and lower arc crust (Collins et al., 2020). This process produces the voluminous intermediate –
912 felsic magmas with juvenile εHf and mantle-like $\delta^{18}O$ that comprise the southern CMB. B:
913 Voluminous flare-up magmatism produces a dense, unstable arc residue that delaminates. Arc root
914 removal causes a shift in the mantle corner flow, leading to trenchward arc retreat. Because the arc
915 migrates back into now-depleted mantle lithosphere, it enters a lull phase and magmas are
916 emplaced into thinned arc lithosphere. WR – Wrangellia; ST – Stikine.

Figure 1: Sample location map

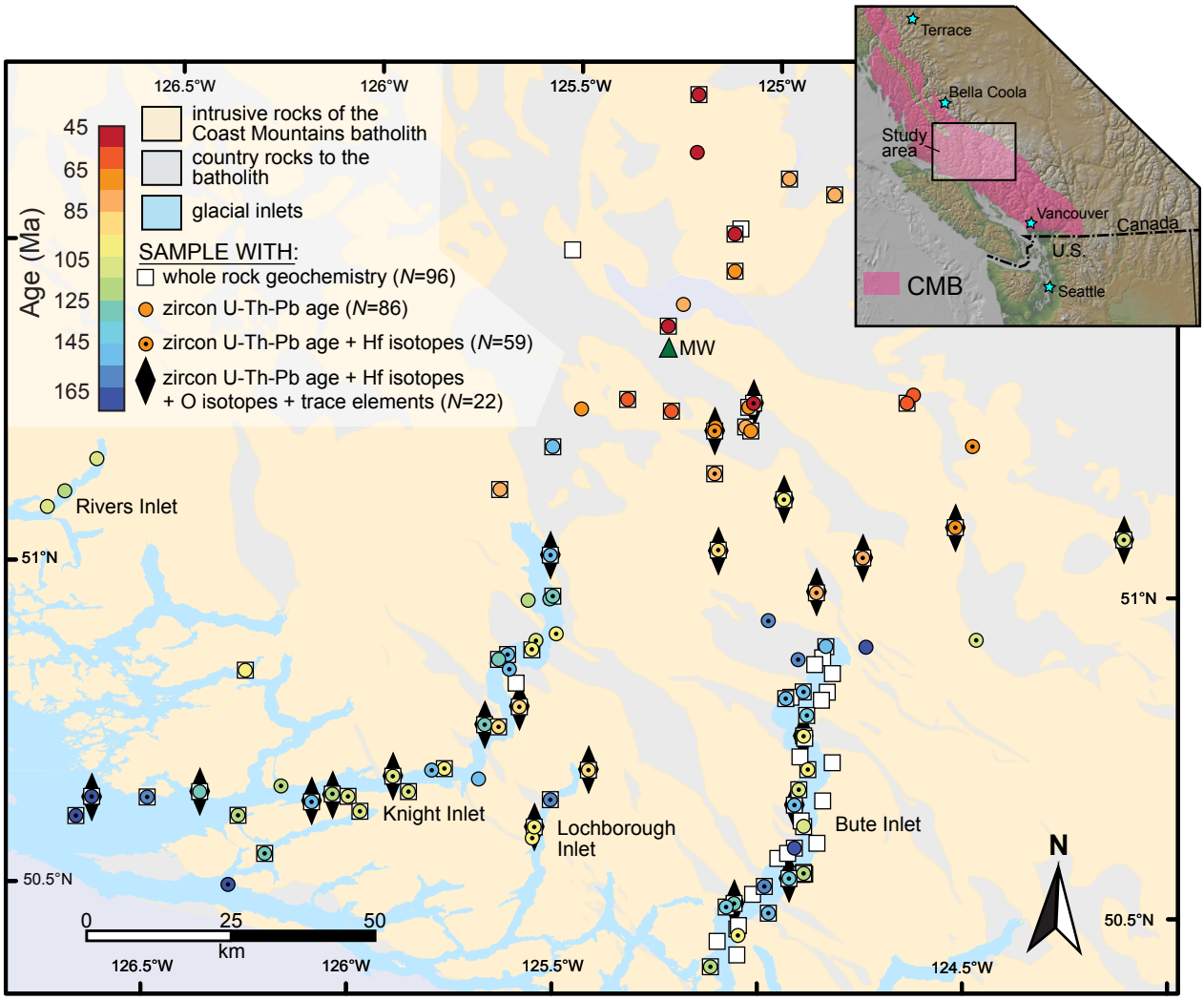

Figure 2: Example U-Pb+Hf data

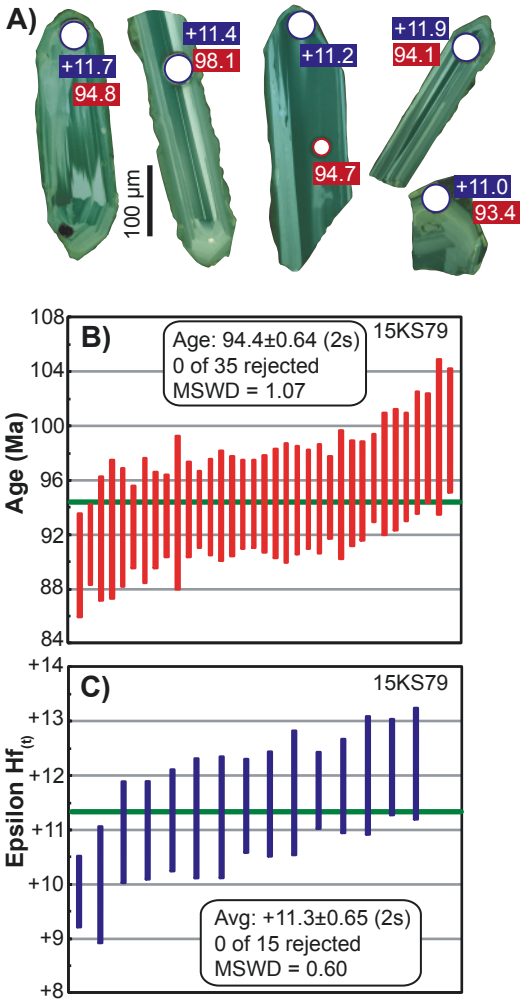

Figure 3: Whole Rock Major Element Data

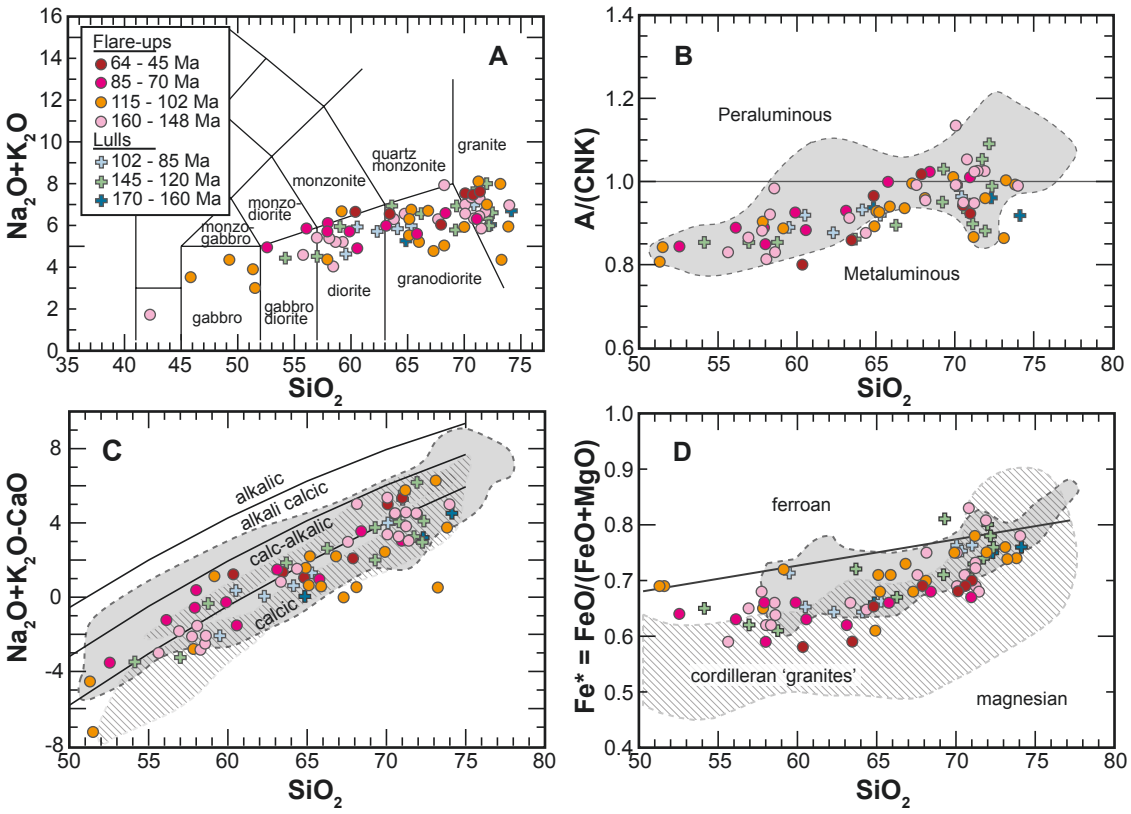

Figure 4: Whole Rock Trace Element Data

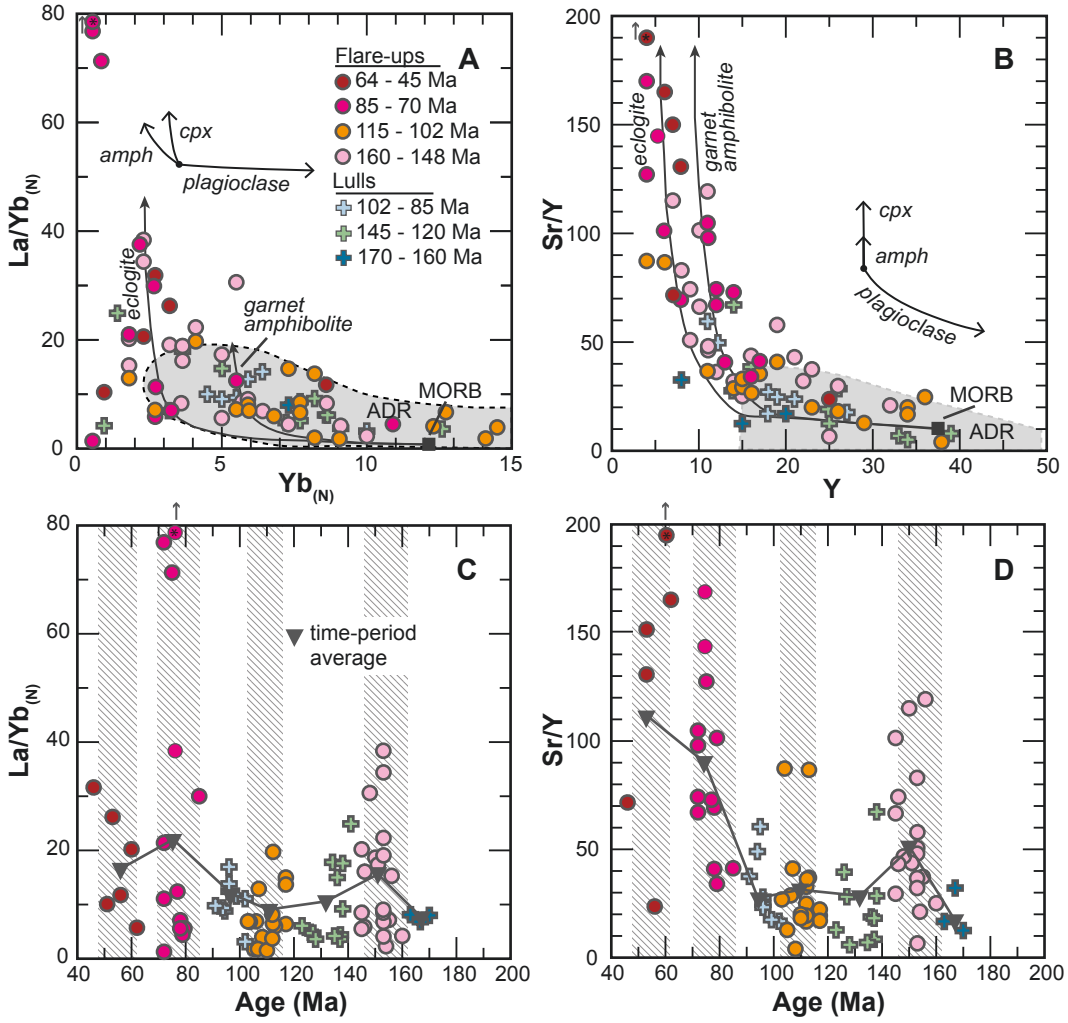

Figure 5: Zircon Hf and O Histograms

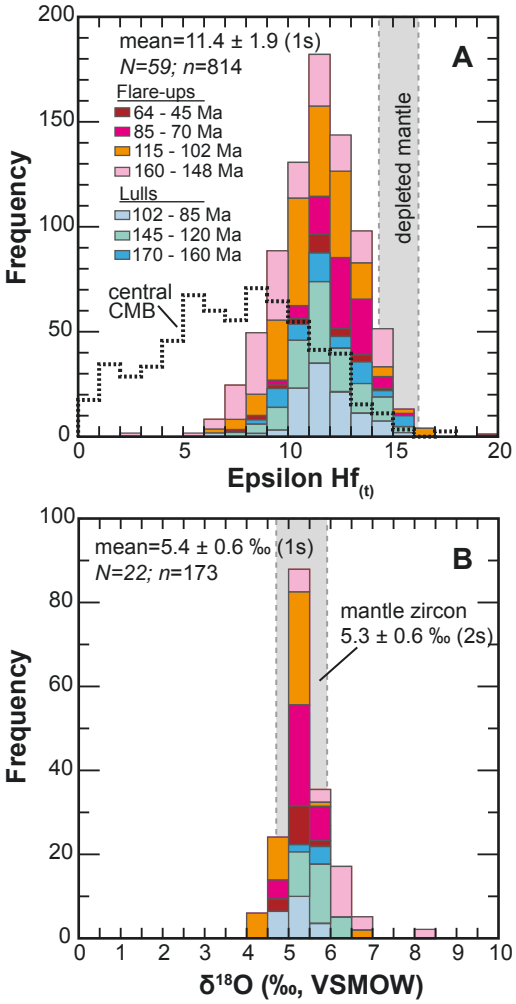

Figure 6: Zircon Hf vs Age

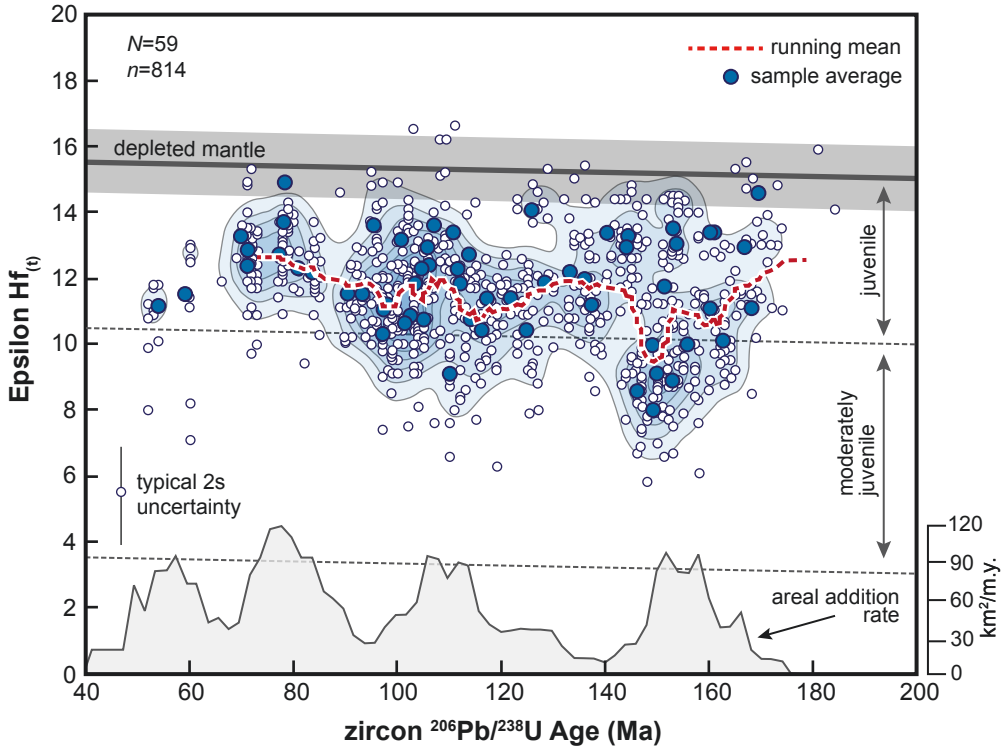

Figure 7: Zircon Trace Element Data

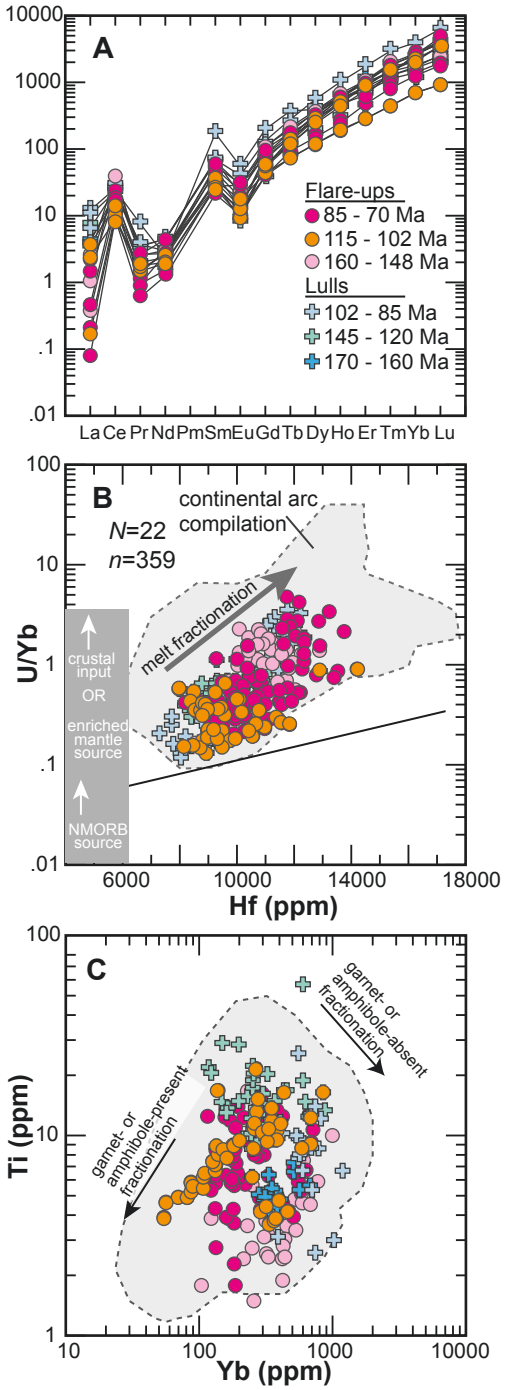

Figure 8: Binary Hf-O Modeling

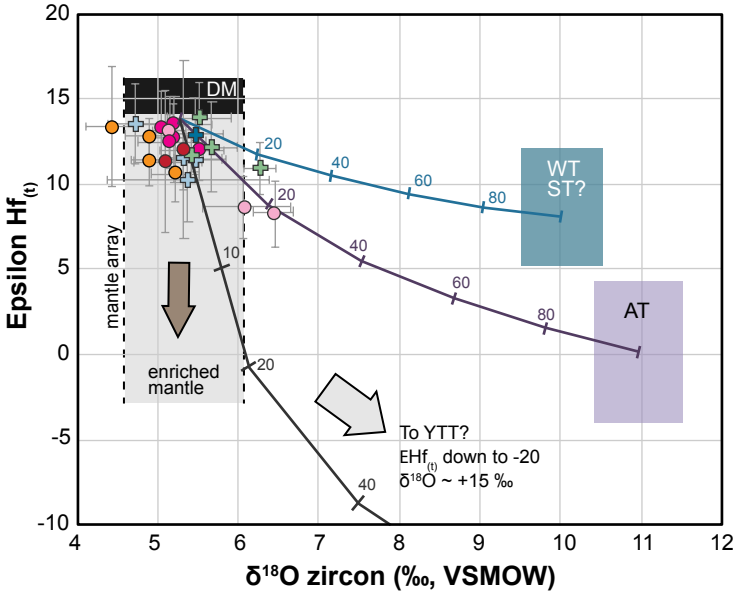

Figure 9: Arc Migration

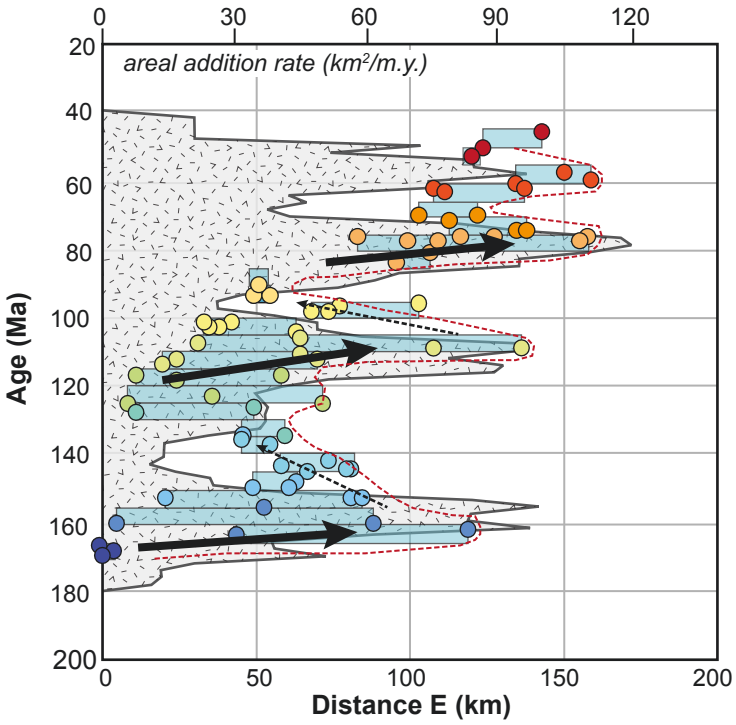

Figure 10: Petrotectonic model